



# Synthesis and studies of the zinc acetate (ZA) crystal for dielectric, nano-photonics and electronic applications

V. Sathiya<sup>1,\*</sup> , K. Suganya<sup>2</sup>, K. SenthilKannan<sup>3,4,\*</sup>, and R. Manikandan<sup>2</sup>

<sup>1</sup>Department of Electronics and Communication Engineering, E.G.S. Pillay Engineering College, Nagapattinam, Tamil Nadu 611 002, India

<sup>2</sup>Department of Chemistry, A.V.V.M Sri Pushpam College (Autonomous—Affiliated to Bharathidasan University, Trichy 620 024), Thanjavur Dt, Poondi, Tamilnadu 613 503, India

<sup>3</sup>Department of Physics/R&D, Edayathangudy G.S Pillay Arts and Science College (Autonomous—Affiliated to Bharathidasan University, Trichy 620 024), Nagapattinam, Tamilnadu 611 002, India

<sup>4</sup>R&D, Phoenix Group, Nagapattinam, Tamilnadu 611 001, India

Received: 7 June 2022

Accepted: 16 July 2022

Published online:

5 August 2022

© The Author(s), under exclusive licence to Springer Science+Business Media, LLC, part of Springer Nature 2022

## ABSTRACT

The ZA are finely full-grown by usual slow evaporation solution growing scheme and the single XRD shows the crystal size as well as the dimension of ZA. The crystal obtained is of white color crystalline precipitate. The crystal system of titled sample is monoclinic, the space group is  $P2_1/c$  and framework of ZA parameters are  $a = 15.097 \text{ \AA}$ ,  $b = 9.238 \text{ \AA}$ ,  $c = 4.7969 \text{ \AA}$ , and beta is  $98.11^\circ$ . The coated ZA is appropriately and finely used for optical-electronic practice improved results for frequency enhancing custom as the standard one more than uncoated value of diodes. Scanning electron microscope analyzed 3000 times magnified image with 10-micron length parameter. The specimen shows uniform mapping of some seed specimen. The ZA structure is explained by the effective computational method. The hardness of different scaling calculates the average value of  $H_V$  index. When the load in grams increases as well as the hardness also tends to be increased, so, the ZA sample has RISE effect with  $n$  as 3.32. The photonic effective nano band gap of ZA is 5.63 eV as well the UV cut-off for nano-ZA is 220 nm; the ZA shows a bluish green light emission all the way through fluorescence; and also the elemental confirmation is done by CHNSO experimental mode analyzing particle size of 52 nm average scaling with TEM configuration.

Address correspondence to E-mail: sathiyav2105@gmail.com; mscgoldmedalist@yahoo.in

## 1 Introduction

In the new years, the interest in combining of organic materials with charge corresponded and exceptionally delocalized  $\pi$ -electron states and developing them as single crystal has expanded extensively, since extremely enormous nonlinear optical susceptibilities have been estimated in a portion of the materials to use them for different applications [1–7]. The electronic properties of organic single crystals have been seriously read and performed for above and beyond 40 years. Top-notch noncentrosymmetric organic single crystals obtain predominant nonlinear optical properties than their inorganic partners because of the delocalization of electrons and donor and acceptor characters [8–16]. The pursuit of new and productive organic materials for nonlinear optical (NLO) measures has been expanded during the most recent years. Dopants are assuming indispensable part in changing the properties of organic single crystals [17–24]. The crystal development field, a part of materials science, has a rich authentic foundation that returns something like a few centuries. It fundamentally manages understanding the basic systems associated with the crystallization interaction and the innovation to create a solitary crystal from some medium in controlled design [25–34]. The field of crystal development envelops a wide range of logical pulling and incorporates as follows. (1) Trial and hypothetical investigations of crystallization measures. (2) The development of crystal under controlled conditions for both logical purposes and industrials, i.e., inorganic and organic mixtures and basic materials just as organic macromolecules [35–42]. Numerous strategies have been created over the course of the years for delivering the size range

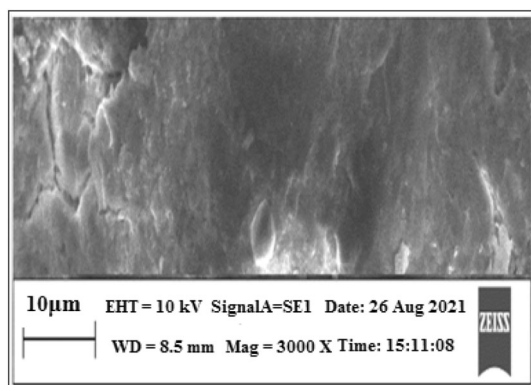


**Fig. 1** SEM micrograph—ZA specimen

**Table 1** Experimental CHNSO data of ZA macrocrystal

Formula/elements	Zn(C <sub>2</sub> H <sub>3</sub> O <sub>2</sub> ) <sub>2</sub>	% of elements
Zn		Not detected <sup>a</sup>
C		26.16
H		3.29
O		34.89
N		Not detected
S		Not detected
Total		64.34

<sup>a</sup>Not detected in CHNSO methodology but present in specimen

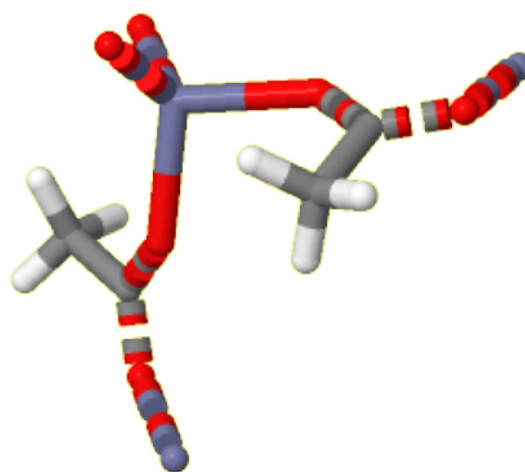


**Fig. 2** Capped stick—ZA specimen

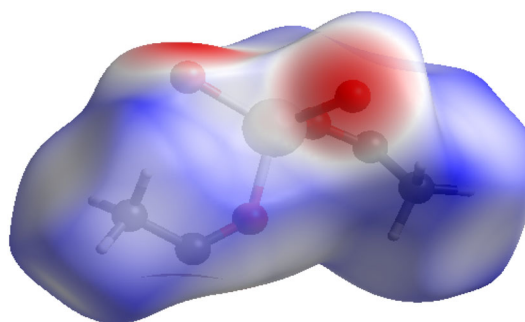


**Fig. 3**  $d_{norms}$ —ZA specimen

for which it fluctuates from the nanometer to meter scale. Much exertion has been spent in planning new atoms and working on sub-atomic nonlinearities that would advance better noncentrosymmetric crystal pressing to empower simpler development [43–52]. Nonlinear optical (NLO) crystals with high second-order NLO efficiencies and upfront in the noticeable and bright ranges are needed for different gadgets in

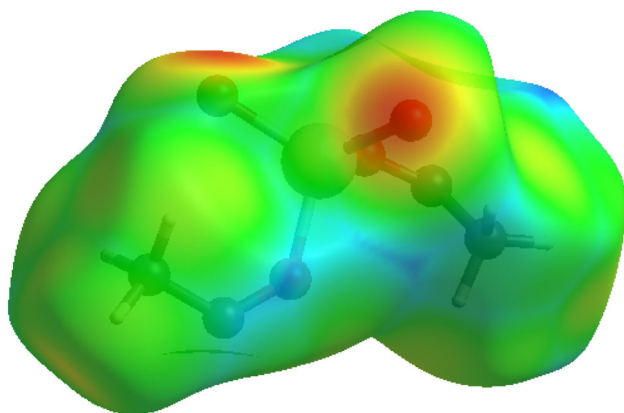


**Fig. 4**  $d_t$ —ZA specimen

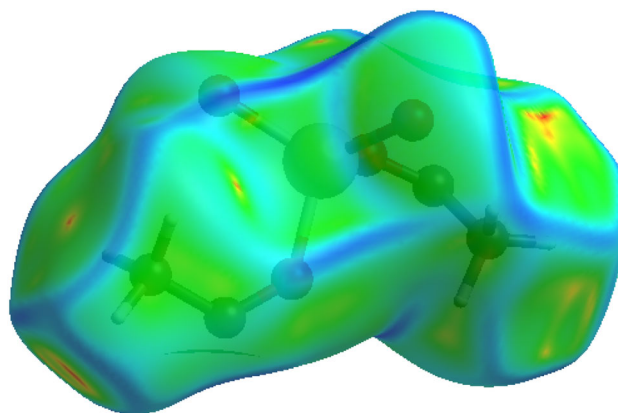


**Fig. 7** Curvedness—ZA specimen

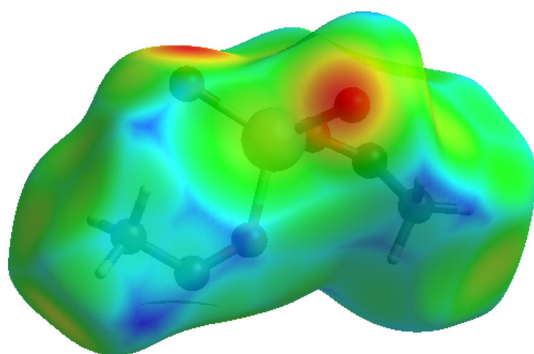


**Fig. 5**  $d_e$ —ZA specimen

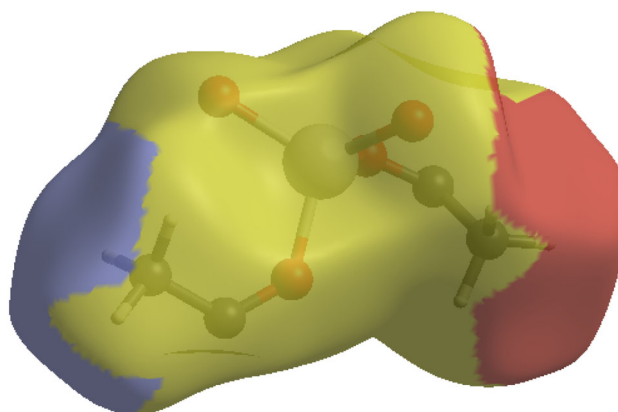


**Fig. 8** Fragment patch—ZA specimen

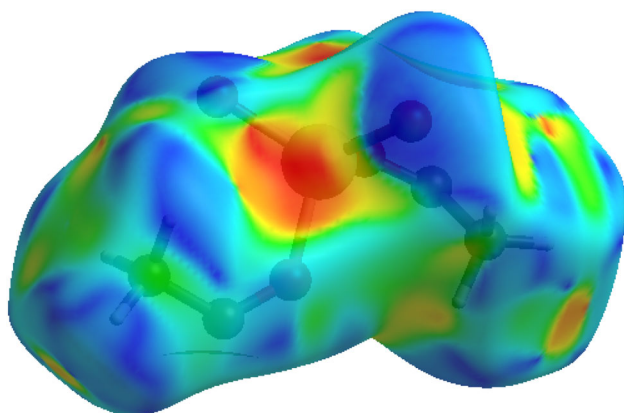


**Fig. 6** Shape index—ZA specimen

the field of optoelectronics and photonics [53–60]. Zinc acetic acid derivation has not many uses beside dietary and restorative applications. It has been utilized in capsules for treating the normal virus. Zinc acetic acid derivatives can likewise be utilized to treat zinc insufficiencies [21, 61–63]. Zinc acetate derivation is a white covering strong assembly of the structures; ZA is an astringent and irritant depending

on minimal to maximum concentration; it is the best anti-bacterial tool [64–73].

### 1.1 Synthesis

ZA is purchased from Sigma-Aldrich-383317 with cis557-34-6 EC#209-170-2, is properly soluble in water, and is a white crystalline specimen obtained 17.5 days after proper rinsing and stirring using magnetic stirrer.

## 2 XRD

The XRD data for anhydrous ZA mainly portray the lattice framework as monoclinicity and  $P2_1/c$ , beta as  $98.11^\circ$ ,  $a$ ,  $b$ , and  $c$  in Å as 15.097, 9.238, and 4.7969 and crystal size of 52 nm by milling, and dimension of ZA as  $10 \times 8 \times 6 \text{ mm}^3$ . The wavelength of 1.5406 Å with a peak positioning of  $40^\circ$  and average size of 52 nm is

**Fig. 9** Finger print effect—ZA specimen

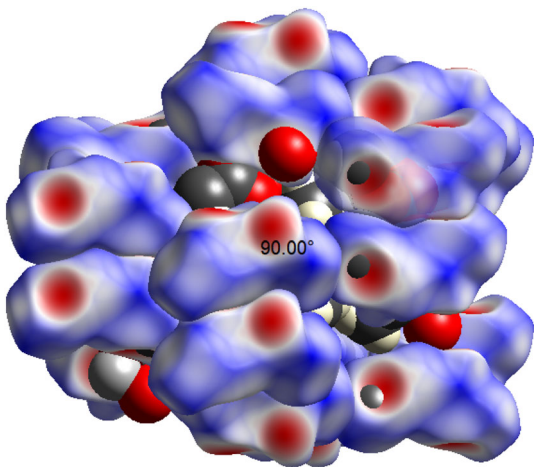
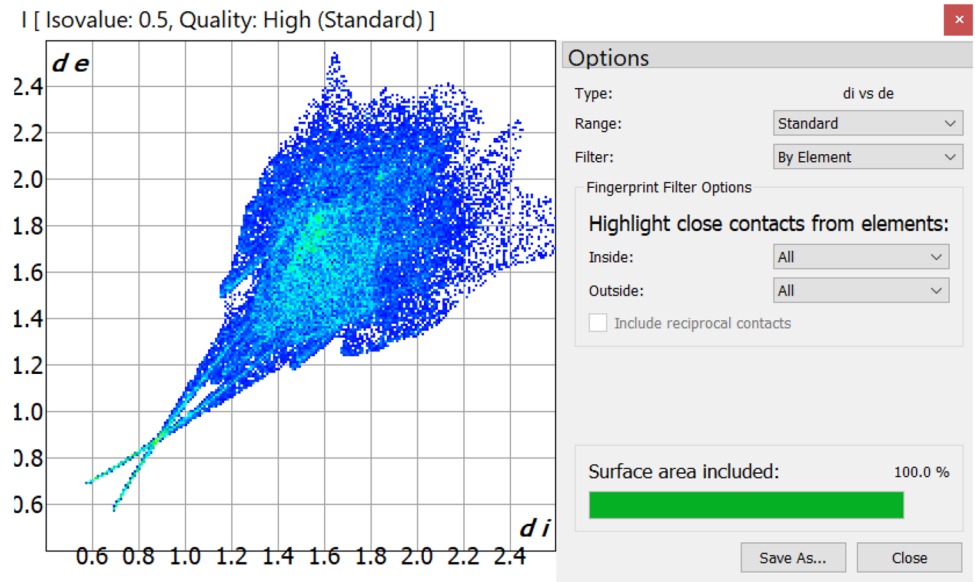
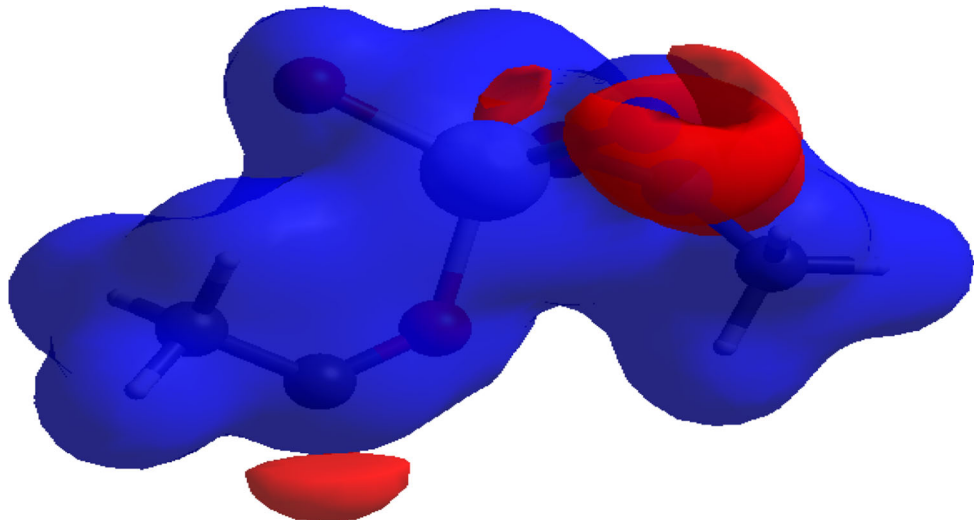


**Fig. 10** Cloning effect of the interactions—ZA cluster specimen

**Fig. 11** Electrostatic potential of ZA specimen



confirmed by the TEM approach as given in the nano influx paper.

### 3 Thin-film influx, frequency enhancer, SEM, and CHNSO of ZA

The thin film-coated filter use of ZA is 4.999 microns for optical-electronic usage and is a better scope for the betterment of results in frequency enhancing use as the standard diodes are of 2Y outcome for input Y as frequency and ZA-coated one has 2.107Y as output and is more than uncoated value. The micrograph of ZA analyzed properly by Zeiss-SE1 with HT 10 kV with a width lie of 8.5 mm and 3000 times magnified



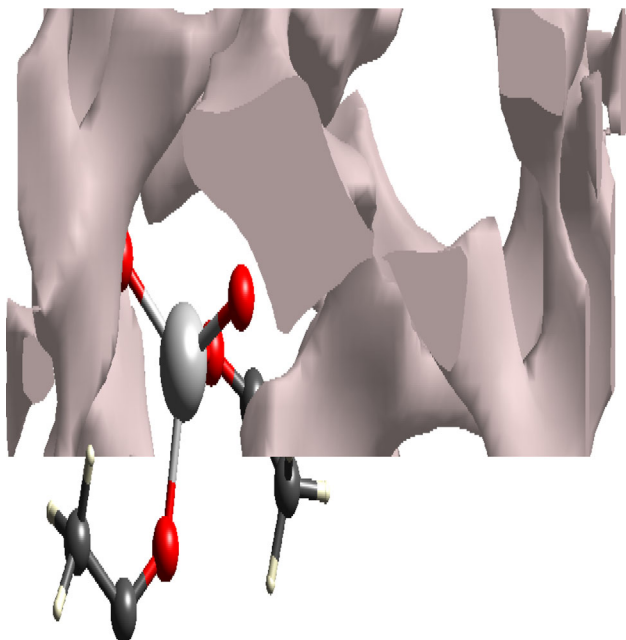


**Fig. 12** Void effect—ZA specimen

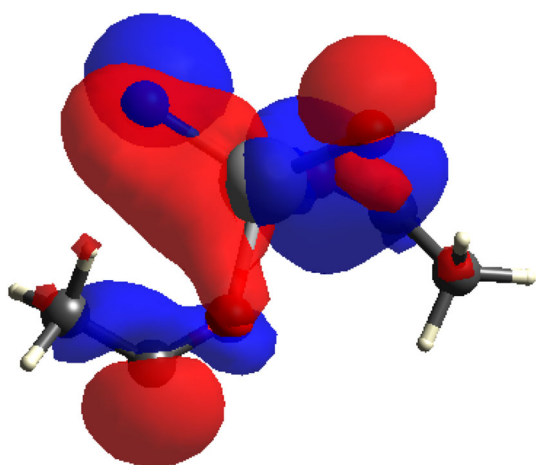


**Fig. 13** HOMO-1 of ZA specimen

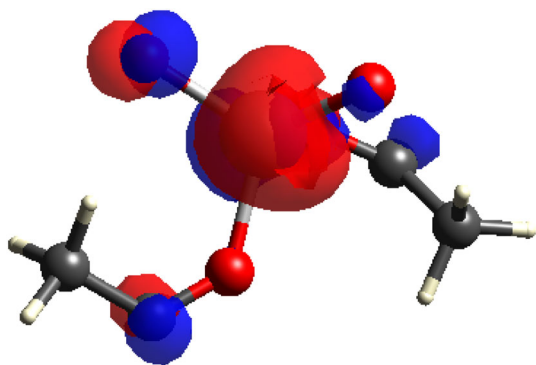


**Fig. 14** LUMO+1 of ZA specimen

image with 10-micron length parameter shows that ZA is having some separated island and some seed specimen is shown inside with uniform mapping and without foremost failing as properly and indicatively allusion as shown in Fig. 1. The composition of elements present in the grown crystal is represented in a fine manner by CHNSO analysis for C, H, and O and the % of 26.16, 3.29, and 34.89 leading to total of 100% including Zn and without it as 64.34% correspondingly without N and S as are not present in titled crystal as shown in Table 1.

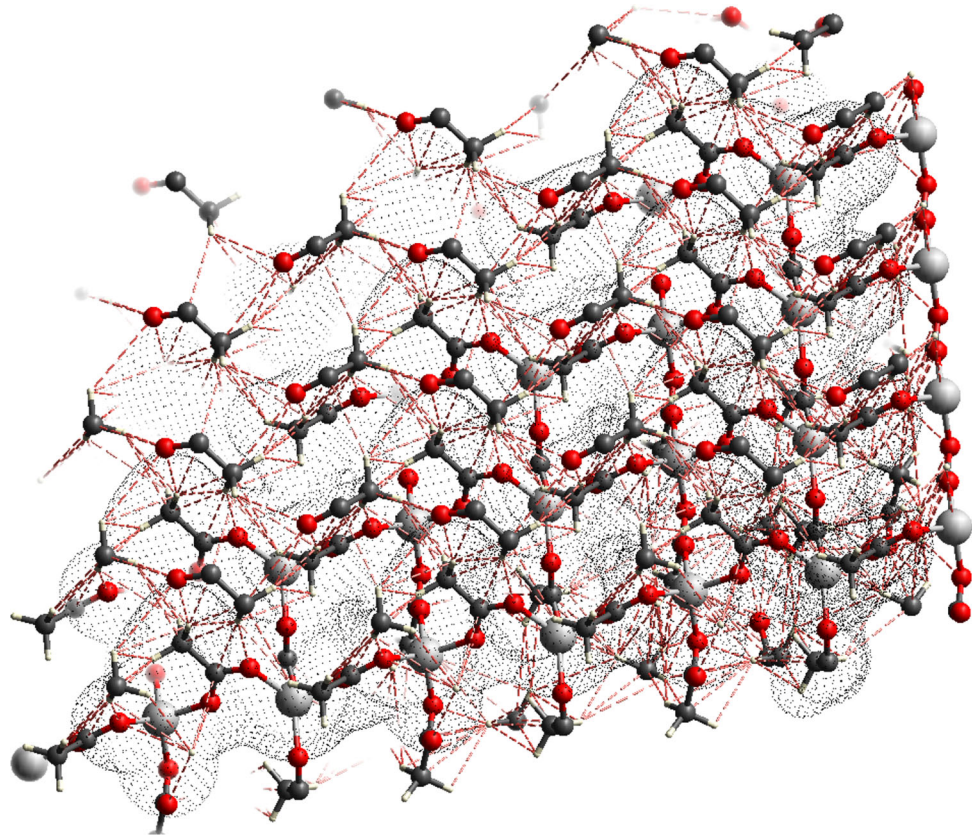
#### 4 Computational

Figure 2 represents the capped stick profile of ZA material. Figures 3, 4, and 5 represent the d spacing, internal, and external interaction energy representation of ZA specimen. Figure 6 represents the indexing profile of the shaping model of ZA and portrays the nonlinearity—NLO effectiveness of the grown specimen for opto-electronic due to the electron affluent and deprived zones in shaped indexed profile. Figure 7 represents the curvedness impact of ZA. Figure 8 shows that the fragmented patch of ZA specimen is ported in a defined manner. In Figure 9, the finger print effect as well as the inside and outside contour of ZA specimen is mentioned. The cloning impact as well as the interactions of multiple atomic representations with  $90^\circ$  portrayal is well defined in Fig. 10. The electron rich and poor zones in the ZA profile is mentioned in Fig. 11. Wide space plays a very vital role in a particular material and here Fig. 12 represents the wide effect. Homo-1 and Lumo+1 are defined in Figs. 13 and 14 for the energy representation. Figure 15 represents the cluster of ZA specimen. Figure 16 represents the dotted mapping of ZA specimen and Fig. 17 represent  $4 \times 4 \times 4$  unit cell generation in three-dimensional effects of ZA sample. Figure 18 portrays the  $5 \times 5 \times 5$  matrix of ZA cluster with void spacing consequence.

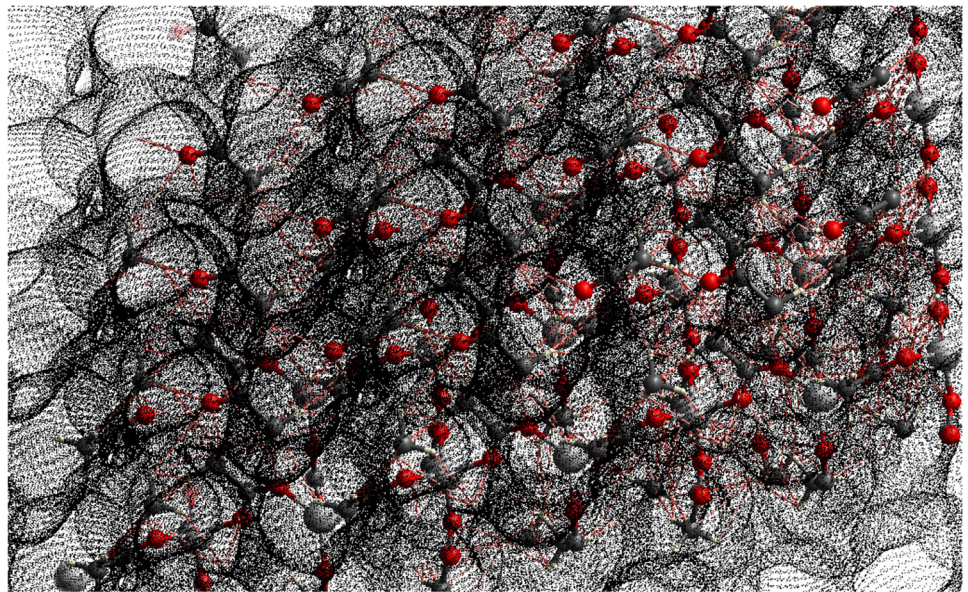
#### 5 Hardness, NLO

The hardness profile for the microhardness effect of ZA is mentioned as shown in Table 2. The hardness of different scaling of 25 g, 50 g, and 100 g are well portrayed with the average value of  $H_V$  index in  $\text{kg}/\text{mm}^2$  as 52.6, 65.2, and 91.9, respectively. So,

**Fig. 15** 3D cluster of ZA specimen



**Fig. 16** 3D cluster-dotted mapping of ZA specimen



when the gram increases the hardness profile also gets increased, accordingly a ZA sample is having high index profile of hardness and it is with a RISE effect and is shown in Figs. 19 and 20 and  $n$  is 3.32; the SHG–NLO efficiency of ZA is well measured by Kurtz methodology and is 1.24 times than KDP.

## 6 Electrical analysis of zinc acetate nanoparticles

In current years, nanoparticles are emerged as a promising alternate in the field of electronics. As the magnetic and electrical properties of nanomaterials



**Fig. 17** 3D effect of  $4 \times 4 \times 4$  unit cell generation of ZA sample

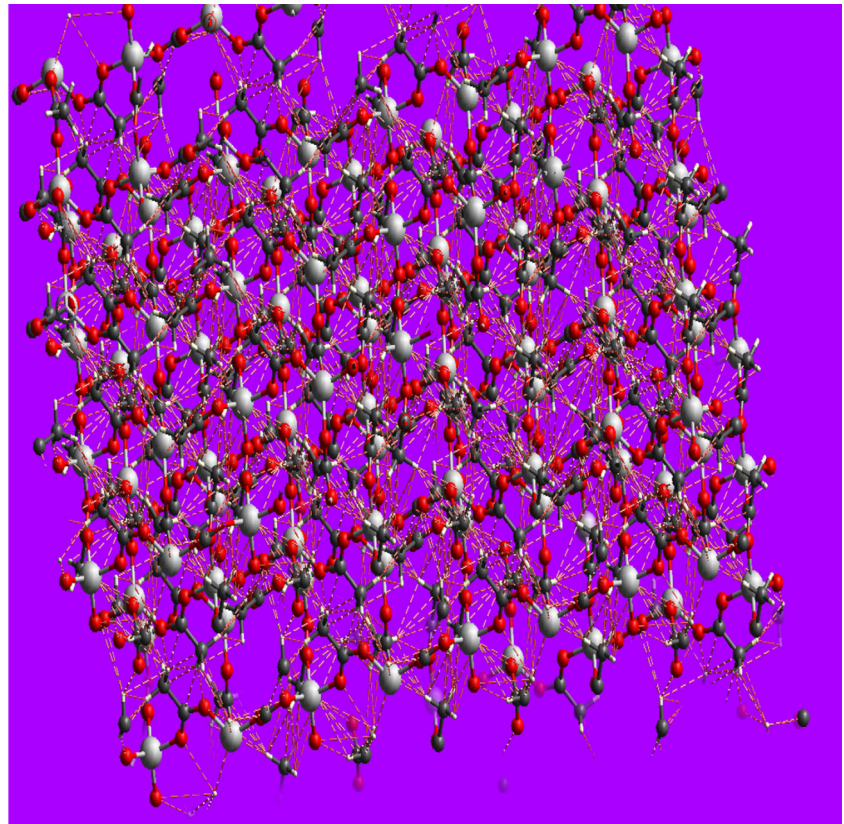


**Fig. 18**  $5 \times 5 \times 5$  matrix of ZA cluster with void spacing effect

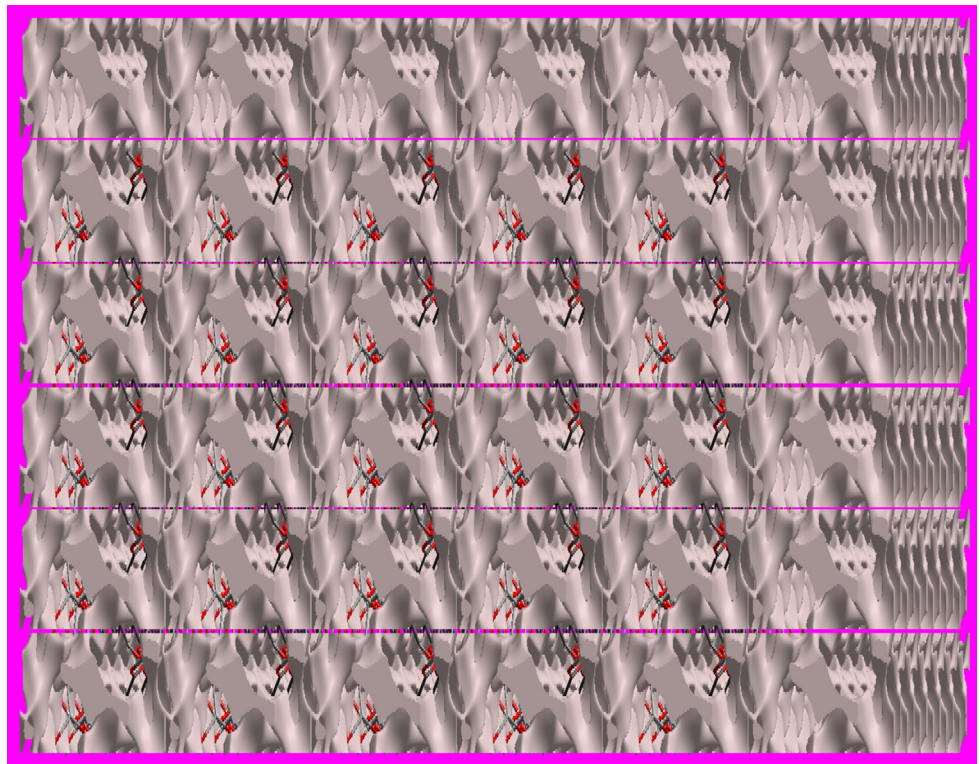


**Table 2** Hardness interactions of ZA crystals

Test Mode : Vickers Hardness Test / ACIC-St. Joseph's College  
 Sample Name : ZA

**Load: 25g**

S.No	L1	L2	Hv in kg/mm <sup>2</sup>
1	26.75	30.89	52.3
2	26.95	30.64	52.9

**52.6****Load: 50g**

S.No	L1	L2	Hv in kg/mm <sup>2</sup>
1	35.72	39.52	64.5
2	35.69	39.76	65.9

**65.2****Load: 100g**

S.No	L1	L2	Hv in kg/mm <sup>2</sup>
1	42.52	46.38	91.8
2	42.58	46.85	92.0

**91.9**

are entirely different from that of their bulk counterpart, it is important to study their electrical response over wide range of temperature and frequency to find their usage in different fields of science [74]. Changes in particle size, shape, and

boundaries were accused for changes in dielectric characteristics [75].

Materials with high dielectric constant with less loss factor are of unique importance [74, 75]. In our present study, we compressed the as-prepared zinc



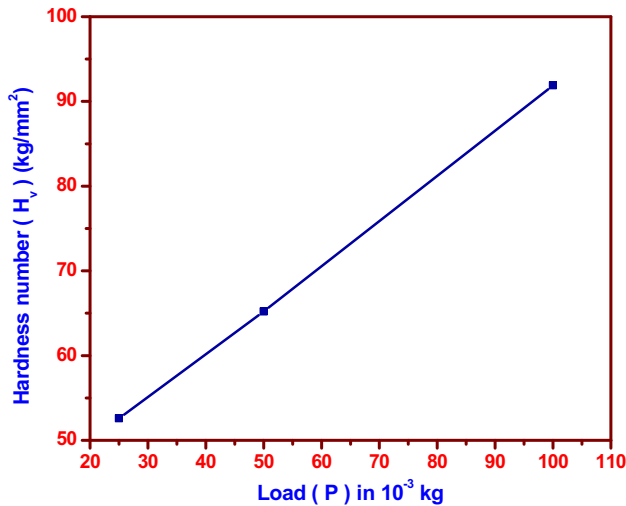


Fig. 19 Hardness profile of ZA

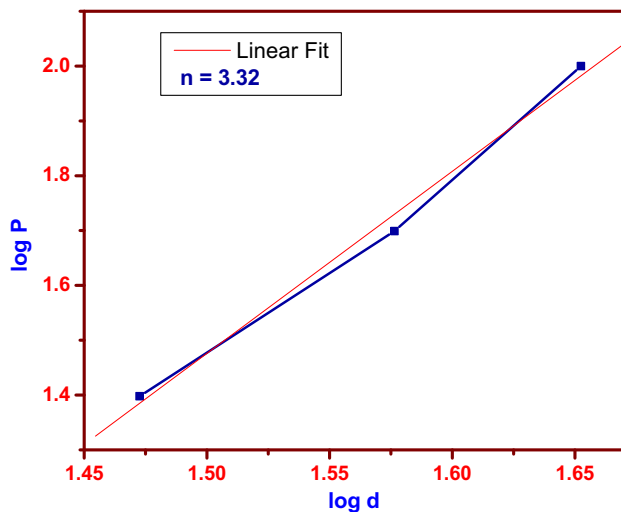


Fig. 20 Hardness profile with linear fitting silhouette of ZA

acetate Np as pellets by applying a pressure of 2 tons using hydraulic pelletizer. The obtained pellets were coated with silver paste on the polished surface for providing proper conduction. Silver coated pellets were placed in between the silver electrodes of the two-probe set-up, which is maintained under constant temperature using a processor controlled digital oven with accuracy of  $\pm 0.05$  °C. Capacitance and loss factors were measured for various frequencies over a temperature range of 40–150 °C using Agilent 4284A LCR meter with an accuracy of  $\pm 2\%$  [74, 75].

The real ( $\epsilon_r'$ ) and imaginary ( $\epsilon_r''$ ) part of the dielectric constant of the material is calculated using the following formulas:

$$\epsilon_r' = \frac{C_p t}{\epsilon_0 A}$$

$$\epsilon_r'' = \epsilon_r' \tan \delta,$$

where  $C_p$  is the capacitance of the sample,  $t$  is the thickness of the disk,  $A$  is the surface area of the electrodes, and  $\epsilon_0 = 8.85 \times 10^{-12}$  F/m which is the permittivity of free space.

Variation of real and imaginary part of dielectric as a function of temperature for various frequencies viz., 100 Hz, 1 kHz, 10 kHz, 100 kHz, and 1 MHz are depicted in Figs. 21 and 22. At low frequencies, a combined contribution owing to electronic, ionic, and interfacial polarization can be attributed to the monotonous reduction in dielectric constant with increasing frequency. In the low-frequency region, the dielectric constant low grain ranges are very effective in this region and requires more energy for electron transfer [76–81]. The dielectric constant ( $\epsilon'$ ) of zinc acetate is decreased with increasing frequency and finally it became independent and constant of frequency at higher frequencies. This decrease in  $\epsilon'$  with respect to increase in frequency is caused by high regular reversal of field at the interface, and this decreases the contribution of charge carrier to the dielectric constant, finally it is saturating at higher frequencies leading to dielectric constant [82–84].

Figures 23 and 24 show the dependence of frequency on the dielectric constant  $\epsilon'$  and the dielectric loss  $\epsilon''$  for the prepared sample at different temperatures (40–150 °C). The thermal behavior of zinc acetate in dielectric constant and dielectric loss shows the endothermic peak in region II at 90–130 °C, which is due to mass loss in low percentage which is evident by analyzing the TG graph from [85]. This is due to the exhale of crystalline water and vaporization of absorbed water. The dielectric constant and dielectric loss in region I show the stable and constant flow at various temperatures. This thermal behavior leads to the semiconductor applications for our prepared samples.

## 7 AC conductivity

The study of conductive property is concerned with the storage and scattering of electrical and magnetic energy in materials. Conductors are important in electronics, optics and in solid state physics to

**Fig. 21** Frequency dependence plot of real part of dielectric constant of ZA

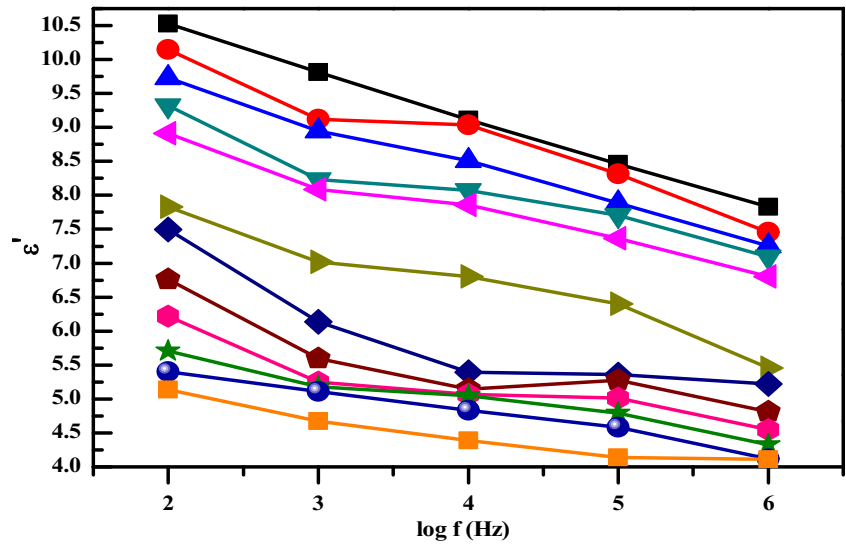


**Fig. 22** Frequency dependence plot of imaginary part of dielectric constant of ZA

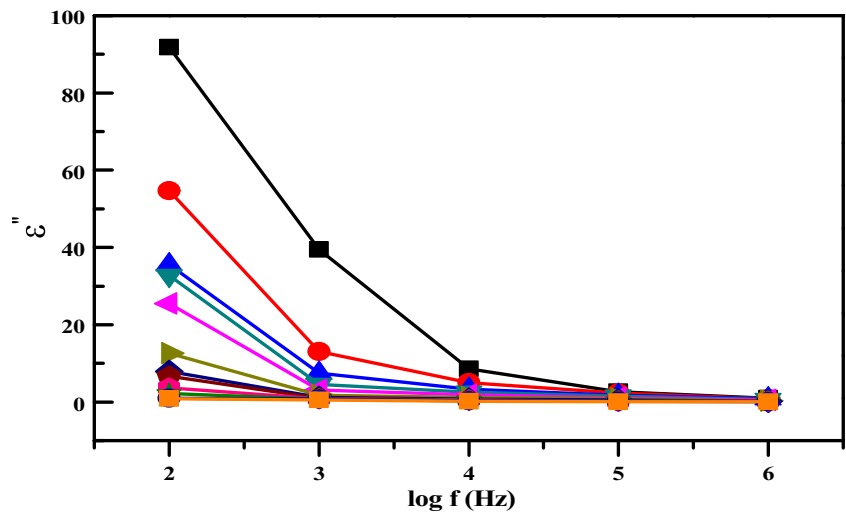


**Fig. 23** Temperature dependence plot of real part of dielectric constant of ZA

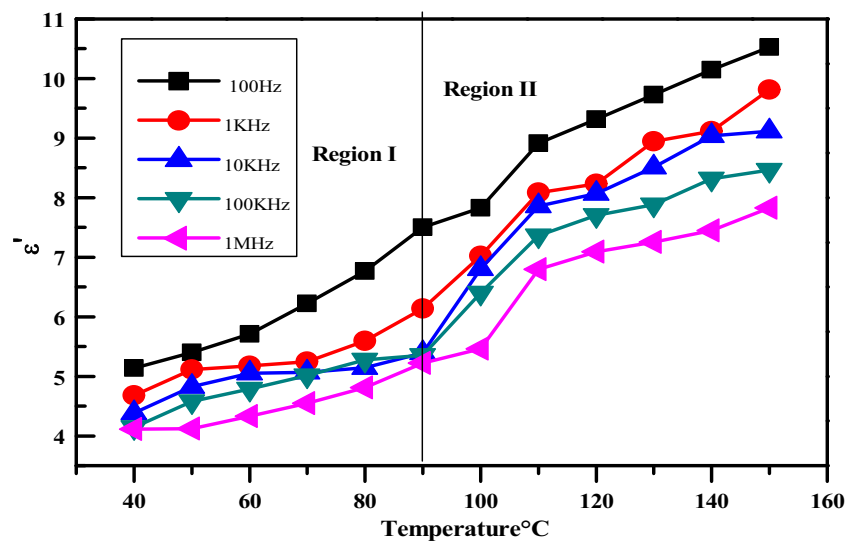


**Fig. 24** Temperature dependence plot of imaginary part of dielectric constant of ZA

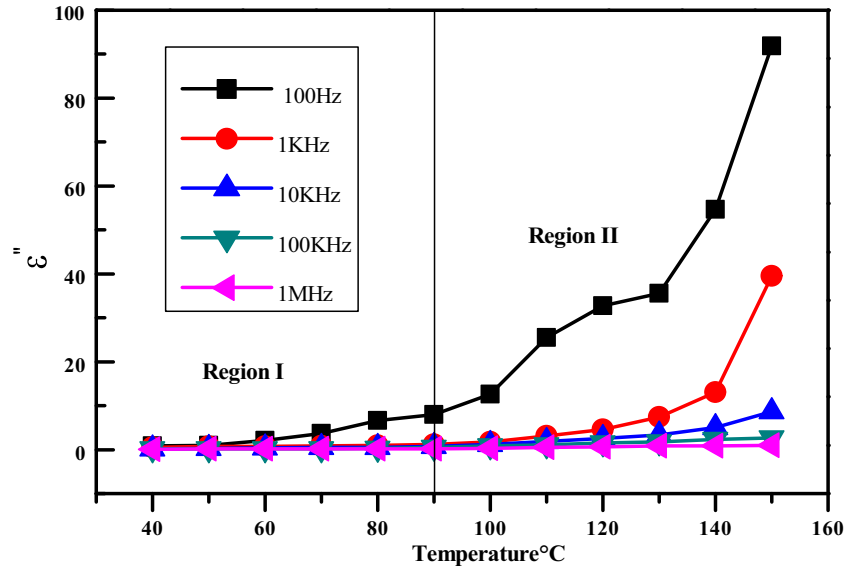
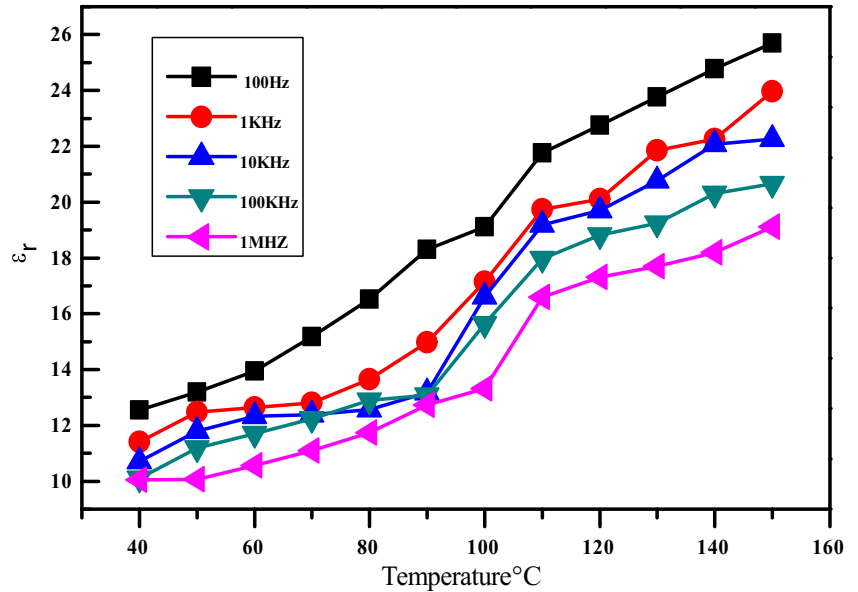


**Fig. 25** Temperature dependence plot of dielectric constant of ZA



explain various phenomena [86]. A commonly used parameter is the dielectric constant of an object, which gives an edge on atoms, ions, and their bonds in matter [87, 88].

The result of dielectric constant with various frequencies and different temperatures of zinc acetate is shown in Fig. 25. From this we clearly understand that the dielectric constant increases with increasing temperature at low frequency and decreases with increasing frequency. The AC conductivity is calculated from the following relation

$$\sigma_{ac} = \omega \epsilon_0 \epsilon_r \tan \delta,$$

where  $\sigma_{ac}$  is the permittivity of free space,  $\omega$  is the angular frequency, and  $\epsilon_r$  is the relative permittivity [89]

Figure 26 illustrates the variation of AC conductivity as a function of temperature and frequency. It was observed that the AC conductivity of the prepared samples increases as the temperature and frequency increase. AC conductivity increases with the transmission contact frequency and is due to small polar bounce [90]. The increase in conductivity can be said with confidence by the optimization mechanism and it appears by the use of an electrical field [91].



**Fig. 26** Temperature dependence plot of AC conductivity of ZA

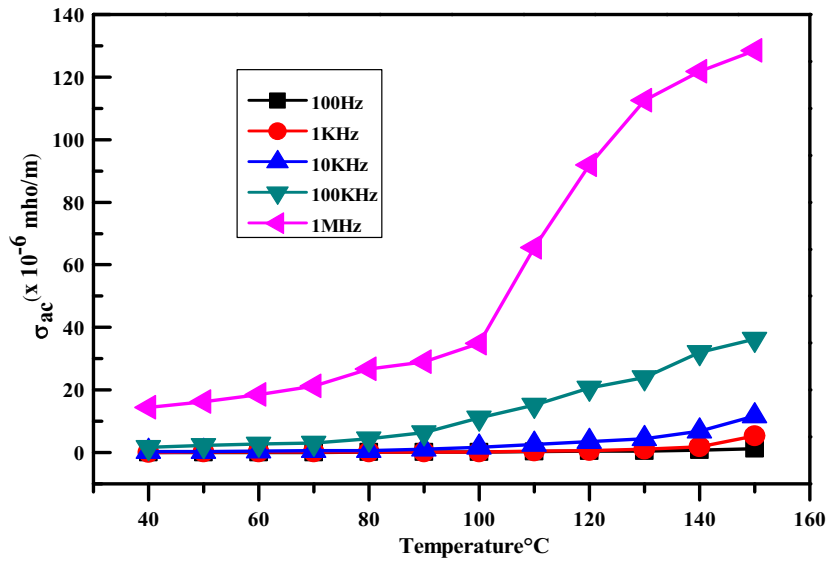
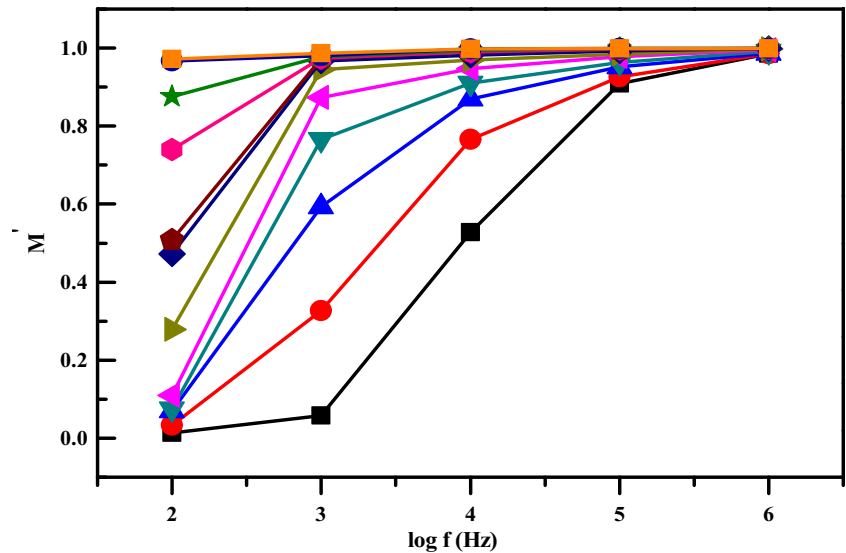


**Fig. 27** Frequency dependence plot of real part of electric modulus of ZA



### 8 Electrical modulus analysis

The electric modulus system is used to analyze the electrical relaxation mechanism in ion-conducting materials [92, 93]. One of the advantages of modulus analysis is that the electrical polarization effects are suppressed. The complex modulus ( $M^*$ ) can be expressed by the following formula [94–96]

$$M^* = \frac{1}{\epsilon' + i\epsilon''}$$

$$M^* = M' - iM''.$$

The values of real ( $M'$ ) and imaginary ( $M''$ ) part of the complex modulus can be obtained by the following relation [97]

$$M' = \frac{\epsilon'}{(\epsilon'^2 + \epsilon''^2)}$$

$$M'' = \frac{\epsilon''}{(\epsilon'^2 + \epsilon''^2)}.$$

From Fig. 27 we observe that the frequency dependence of the real part of electric modulus at different temperatures reaches a maximum value at high frequencies and it approaches low value (nearly zero) at low frequencies. The maximum value at high frequency is due to conductive relaxation process

**Fig. 28** Frequency dependence plot of imaginary part of electric modulus of ZA

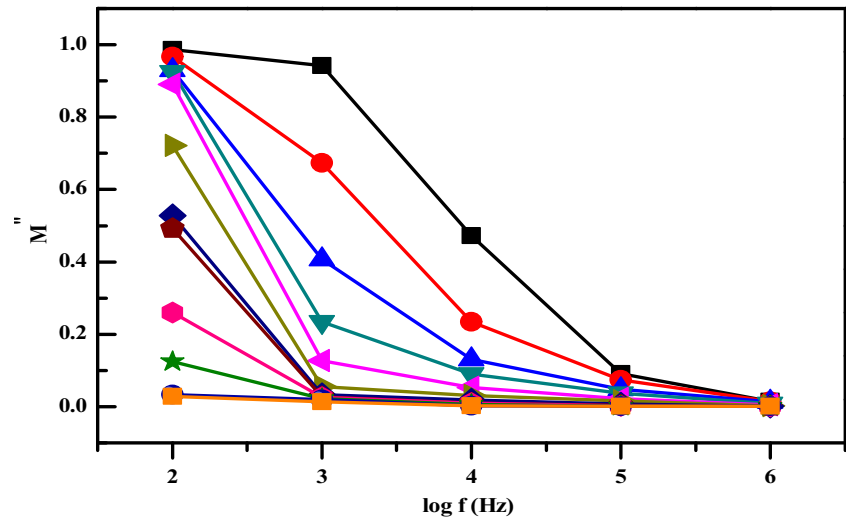
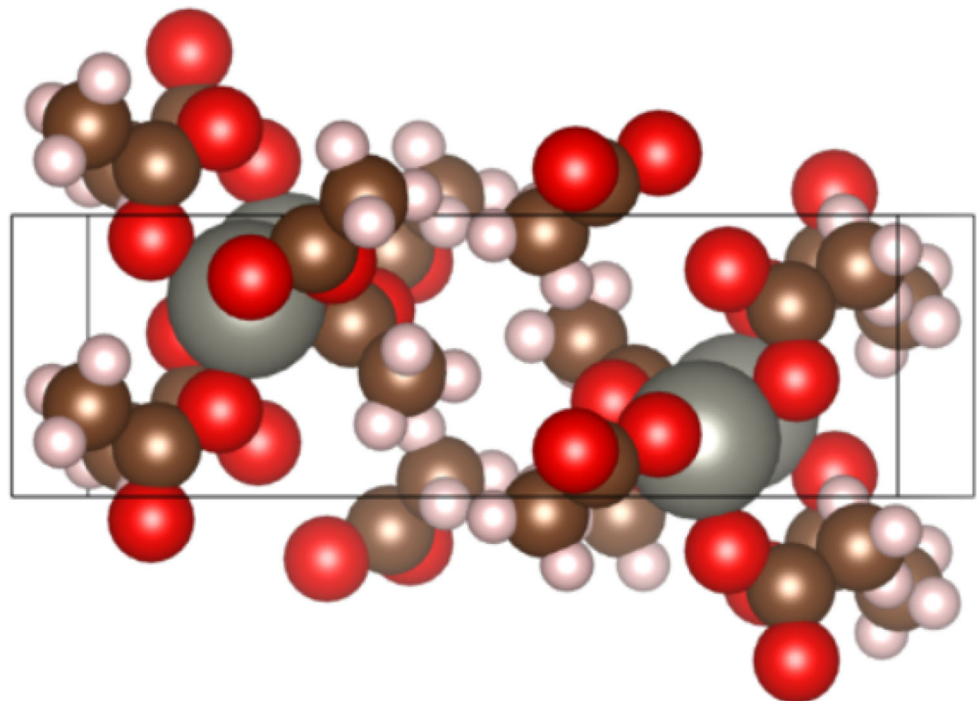


**Fig. 29** Unit cell with space-filled outcome of ZA



[98]. The low values at low frequency indicates that the electric polarization drive a very small contribution [99, 100]. Compared with Fig. 21, this electric modulus shows reverse behavior with the dielectric constant. The frequency dependence of the imaginary part of electric modulus at different temperature is shown in Fig. 28. The relaxation process is obtained at high frequency and is constant with increasing frequency. The extension of plotted peaks shows a semicircular arc and which gives the existence of large relaxation process [101]. The smaller the radius of the semicircular curve the greater the capacity.

## 9 Unit cell, PXRD-simulated, and UV-Vis fluorescence data

The space-filled unit cell and Fourier model of ZA are shown in Figs. 29 and 30 by software, the simulated pattern of Powder XRD data for  $10^\circ$ – $100^\circ$  versus  $10$ – $100$  intensity data is shown in Fig. 31, and the thermal projection of ZA is properly portrayed in Fig. 32 for the atomic arrangement; Table 3 discloses the lattice data by theory and practice of ZA for comparative outcome.

Fig. 30 Fourier effect of ZA

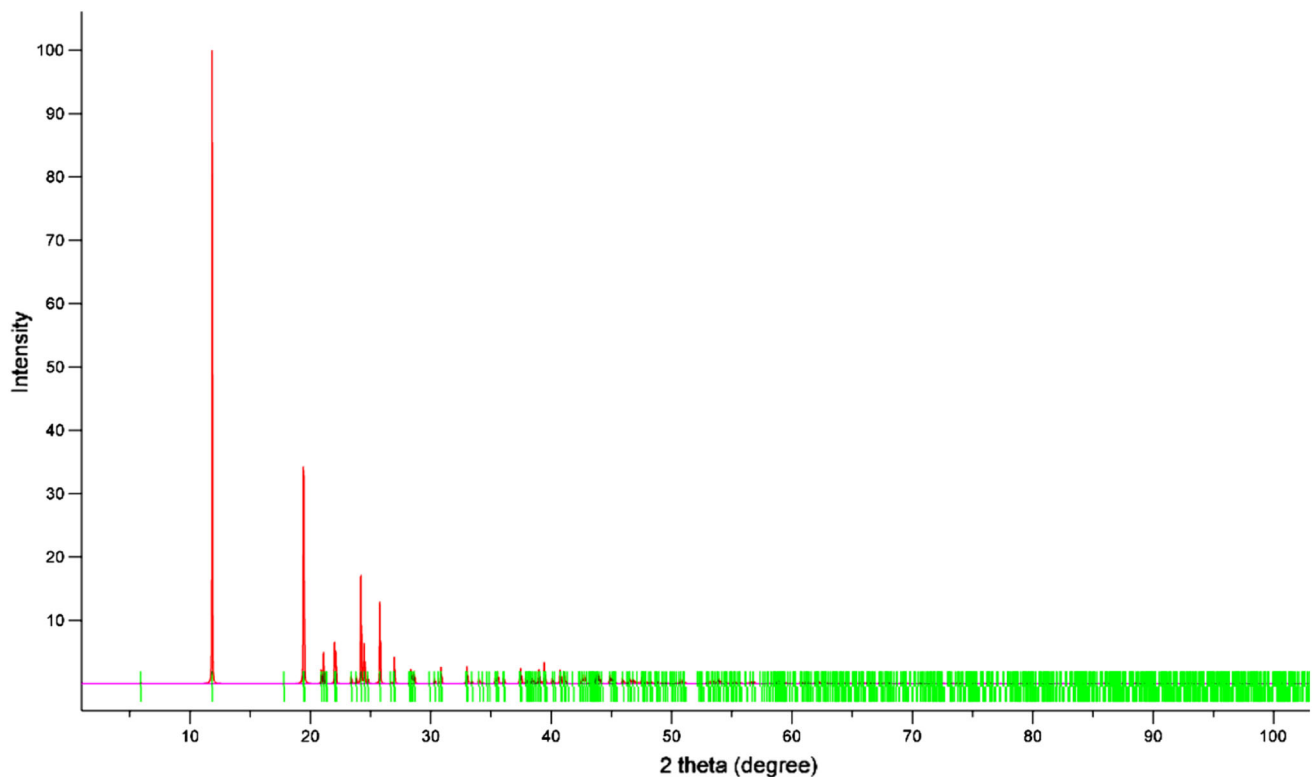
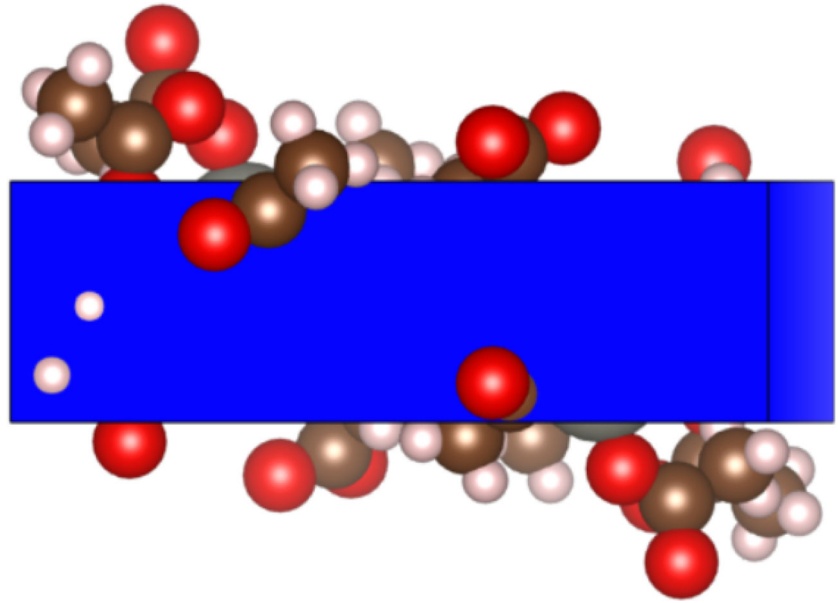
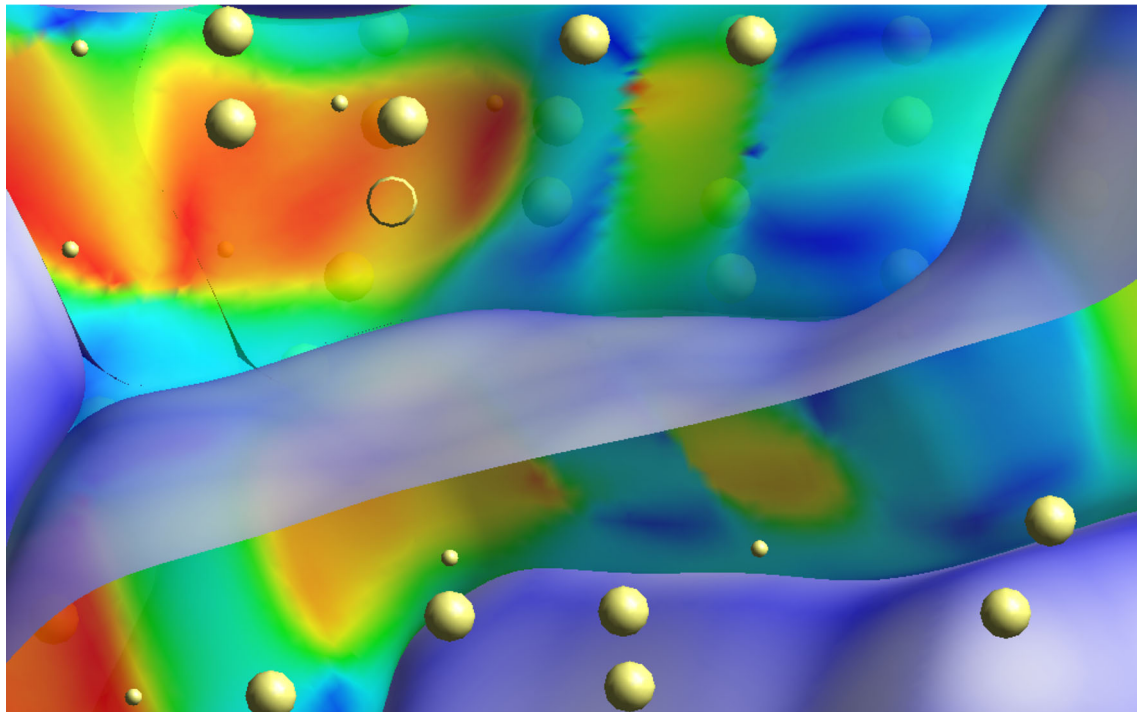


Fig. 31 PXR D—simulated effect of ZA

The UV spectral cut-off wavelength for nano-ZA (the macro which is milled for 52 nm) is 220 nm by Fig. 33 and proper counter verification of the same for band gap in eV as 5.63 as mentioned in Fig. 34 specifies the nano-photonic utility from Tauc's plot. The refranged wavelengths corresponding to

versatile scaling are 505 nm and 481 nm, proving the bluish green light emission through fluorescence corresponds to the energy impact of 2.5777 eV and 2.4520 eV by Fig. 35. The computational impact is mainly by the use software for interactions and fabrications [102, 103]





**Fig. 32** Thermal projection effect of ZA

**Table 3** XRD part of data for geometrical bound of ZA using Gaussian software

Parameters	Theoretical data	Parameters	Theoretical data
ZnC1–ON3	1.961	CN1–CN2	1.520
ZnC1–ON2	1.969	CN3–ON4 <sup>iv</sup>	1.284
ZnC1–ON4	1.975	CN2–HN2A	0.978
ZnC1–ON1	1.979	CN4–HN4C	0.978
ON1–CN3	1.280	ON1–CN3–CN4	122.3
ON2–CN1	1.285	ON4 <sup>iv</sup> –CN3–CN4	119.8
ON3–CN1 <sup>i</sup>	1.276	CN1–CN2–HN2A	111.7
ON4–CN3 <sup>ii</sup>	1.282	HN4A–CN4–HN4B	111.7
CN1–ON3 <sup>iii</sup>	1.276	HN4A–CN4–HN4C	111.7
ON3–ZnC1–ON2	109.74	HN4B–CN4–HN4C	111.7
ON3–ZnC1–ON4	114.9	ON1–ZnC1–ON4–CN3 <sup>ii</sup>	169.6 (2)
ON2–ZnC1–ON4	119.9	ZnC1–ON2–CN1–ON3 <sup>iii</sup>	168.6 (2)
ON3–ZnC1–ON1	113.9	ON3 <sup>iii</sup> –CN1–ON2	122.1
ON2–ZnC1–ON1	102.9	ON3 <sup>iii</sup> –CN1–CN2	118.3
ON4–ZnC1–ON1	105.8	ON2–CN1–CN2	123.3
N3–ON1–ZnC1	129.8	ON1–CN3–ON4 <sup>iv</sup>	122.3
CN1–ON2–ZnC1	134.5	ON3–ZnC1–ON1–CN3	176.6
CN1 <sup>i</sup> –ON3–ZnC1	119.5	ON4–ZnC1–ON2–CN1	126.3
CN3 <sup>ii</sup> –ON4–ZnC1	113.6	ON2–ZnC1–ON3–CN1 <sup>i</sup>	168.2

CN—Carbon; ON—Oxygen; ZnC—Zinc; HN—Hydrogen

**Fig. 33** Absorbance spectrum effect of nano-ZA

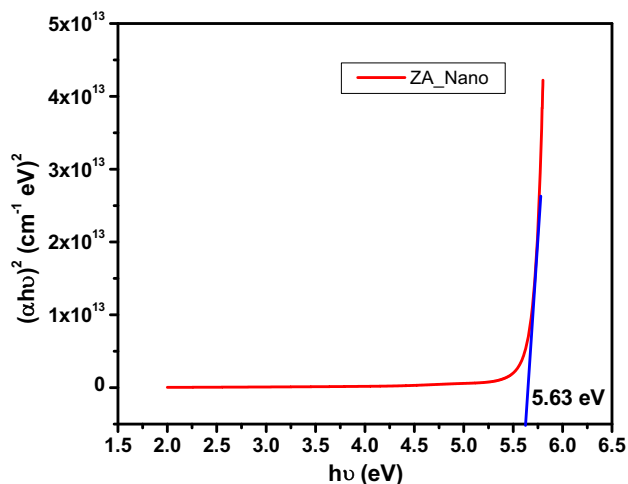
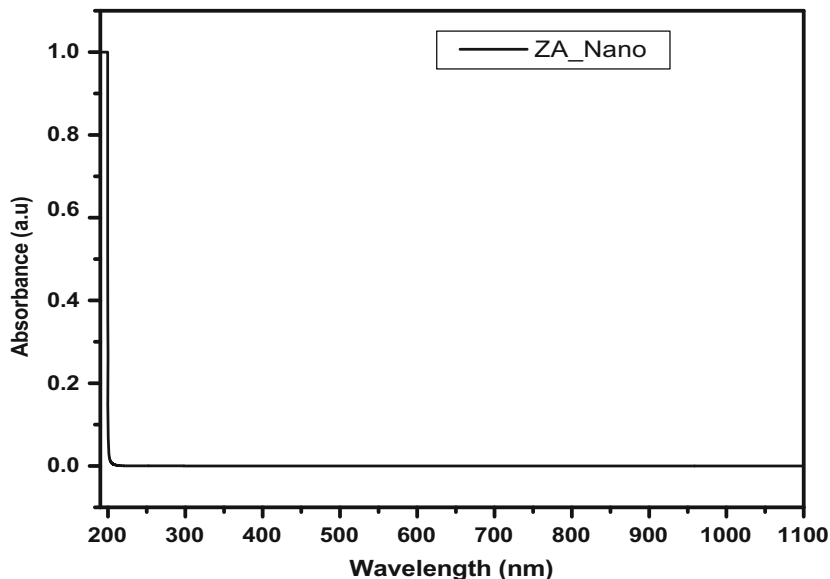


**Fig. 34** Tauc's plot of nano-ZA

## 10 Conclusion

The ZA crystals are grown successfully by slow evaporation solution growth method. The lattice parameters are identified using single-crystal XRD methodology, the space group is  $P2_1/c$  and lattice parameters is  $a = 15.097 \text{ \AA}$ ,  $b = 9.238 \text{ \AA}$ ,  $c = 4.7969 \text{ \AA}$ , and beta is  $98.11^\circ$ . The highest yield is obtained of ZA crystal for white crystalline powder and confirming

the elements by experimental CHNSO mode and macro one is converted by ball milling mode to nano of 52 nm confirmed by TEM approach. The ZA crystals are monoclinic in nature. The thin film influx-coated ZA used for optical-electronic usage better results for frequency enhancing usage as the standard diodes more than uncoated value. Scanning electron microscope is analyzed 3000 times magnified image with 10-micron length parameter. Micrograph of ZA is analyzed properly by Zeiss-SE1 with HT 10 kV with a width lie of 8.5 mm and having separated island and seed specimen shown inside with uniform mapping. As well as the computational method is fully explained for the structure of ZA crystals. Structure is represented for capped stick profile and internal and external energy representation and fragmented patch, finger print effect impact, wide effect of Homo-1 and Lumo+1, and energy representation, etc. The hardness of different scaling of 25 g, 50 g, and 100 g is well portrayed with the average value of  $H_V$  index in kg/mm<sup>2</sup> as 52.6, 65.2, and 91.9, respectively. So, when the load increases the hardness profile also gets increased, accordingly a ZA sample is having high index profile of hardness and it is with a RISE effect with the esteem of  $n$  as 3.32. The photonic scheduled ZA is well portrayed by

ACIC  
St. Joseph's College ( Autonomous)  
Trichy-2

Fluorescence - Report  
Date: 9/6/2021

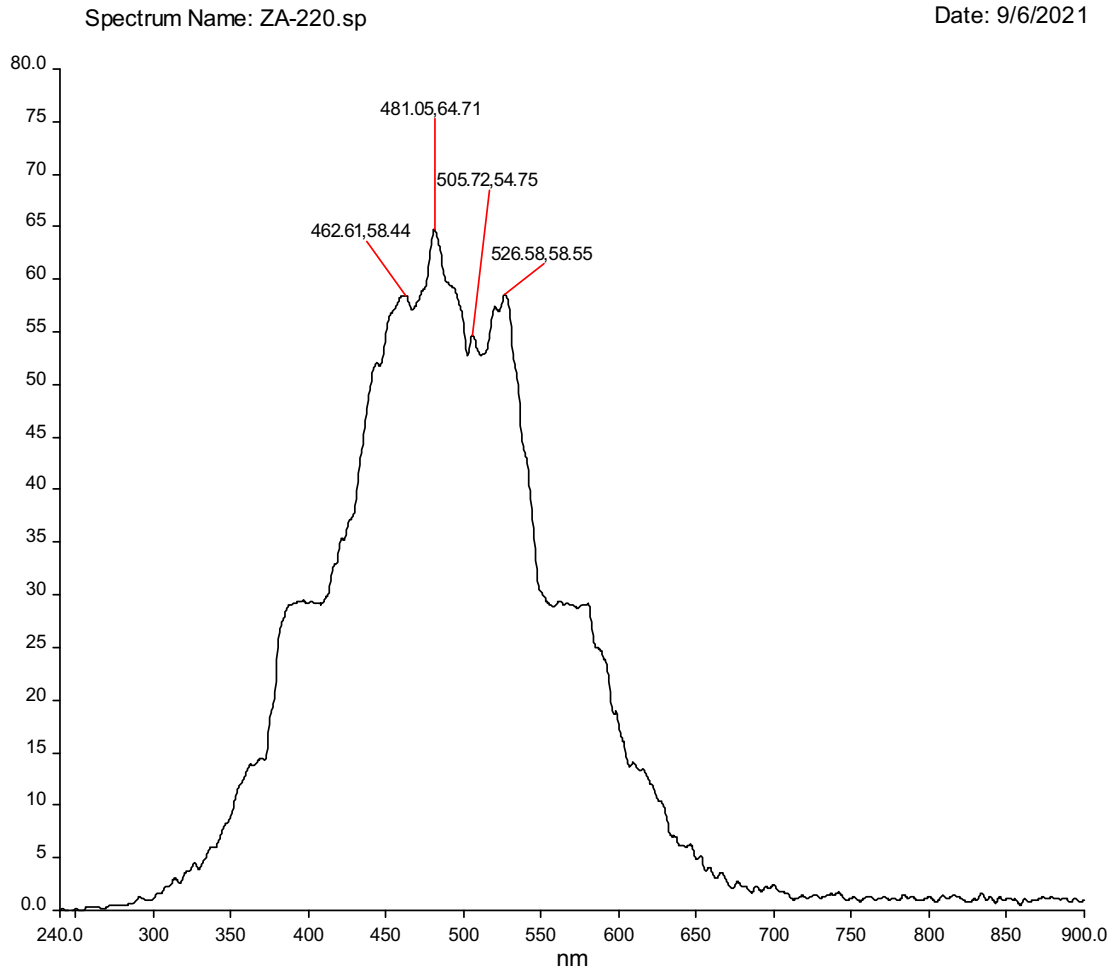


**Fig. 35** Fluorescence spectrum of nano-ZA

5.63 eV, correspondingly the UV cut-off wavelength for nano-ZA is 220 nm, the refranged effect for the bluish green light emission through fluorescence.

### Author contribution

V. Sathiya contributed to electrical analysis. K. Suganya contributed to crystal growth. K. SenthilKannan contributed to overall write up and other studies including interactions and paper responsibility. R. Manikandan analyzed structural and clone effect.

### Funding

The authors have not disclosed any funding.

### Research data policy and data availability statements

Data are not submitted anywhere and all studies performed are presented here; no data separately available in any system or mode.



## Declarations

**Conflict of interest** The authors have not disclosed any competing interests.

**Ethical statement** All authors agreed to proceed and equally contributed; this paper is not presented anywhere for publication.

## References

1. A.G. Quarell, *Nature* **170**, 818 (1952). <https://doi.org/10.1038/170818b0>
2. E.M. Onitsch, The present status of testing the hardness of materials. *Mikroskopie* **95**, 12 (1956)
3. R. Bhuvaneswari, K.S. Murugesan, *Opt. Mater.* **98**, 109431 (2019). <https://doi.org/10.1016/j.optmat.2019.109431>
4. S. Yesuvadian, A. Selvaraj, M.M. Methodius, B. Godavarti, V. Narayanasamy, P.A. Devarajan, *Optik* **126**(1), 95–100 (2015)
5. M. A. Rajkumar, S. Stanly John Xavier, S. Anbarasu, P. A. Devarajan, *J. Phys. Sci.* **2**(1), 1 (2014).
6. M.E. Lines, A.M. Glass, *Principle and Application of Ferroelectrics and Related Material* (Oxford University Press, Oxford, 1997)
7. S.M. Dharmaprakash, P. Mohan Rao, *J. Mater. Sci.* **8**, 1167 (1989)
8. K. SenthilKannan, *Int. J. Eng. Mater.* **7**(4), 310 (2018)
9. E.M. Onitch, *J. Cryst. Process Technol.* **95**, 12 (1956)
10. R. Krishnaveni et al., *Preamble to Biomaterials and its Applications in Science and Technology*, Lulu Publications (2019).
11. S. Gunasekaran, K. SenthilKannan, S. Loganathan et al., *Indian J. Phys.* **87**, 1189 (2013). <https://doi.org/10.1007/s12648-013-0363-8>
12. R. Aarthi, S. Ramalingam, S. Periandy K. SenthilKannan, *J. Taibah Univ. Sci.* **13**(1), 917 (2019).
13. K. SenthilKannan, S. Gunasekaran, K.A. Seethalakshmi, *Int. J. Sci. Eng.* **4**, 2 (2013)
14. N. Kishore, K. SenthilKannan, T. Periyayagi et al., CO and HCHO adsorption on FeOmonowire devices: a DFT study. *Appl. Phys. A* **123**, 706 (2017). <https://doi.org/10.1007/s00339-017-1330-6>
15. P. Saravanan, K. SenthilKannan, R. Divya et al., *J. Mater. Sci. Mater. Electron.* **31**, 4301 (2020). <https://doi.org/10.1007/s10854-020-02985-9>
16. M. Jothibas, et al. *AIP Conference Proceedings* 2162, 020151 (2019). <https://doi.org/10.1063/1.5130361Published>.
17. S. Gnanam et al., *IOP Conf. Series: Mater. Sci. Eng.* **561**, 012086 (2019). <https://doi.org/10.1088/1757-899X/561/1/012086>.
18. R. Krishnaveni et al., *Int. J. Anal. Exp. Modal Anal.* **11**, 8 (2019)
19. K. SenthilKannan, *Int. J. Eng. Math.* **7**, 1 (2018)
20. K. SenthilKannan et al., *Int. J. Chemtech. Res.* **6**, 3187 (2014)
21. K. SenthilKannan, S. Gunasekaran, *Int. J. Frontier Technol.* **3**, 29 (2013)
22. T. Malathi Rekha et al., *Int. J. Appl. Nat. Sci.* **5**, 133 (2018).
23. K. Senthilkannan et al., *Spectroscopic (IR & Raman) studies of picolinium maleate (pm) single crystal*. *Scholars Research Library Archives of Applied Science Research* **5**, 100 (2013)
24. G. Flora et al., *Anti diabetic (AD), stiffness and hardness studies of 2-[4-(Trifluoromethyl) phenyl]-1H-benzimidazole crystals-(TFMPHB) macro and nano crystal*. *Mater. Today: Proc.* (2020).
25. R. Senthilkumar et al., *Anti-diabetic (AD) and hardness profile of 12-(4-Chlorophenyl)-9, 9-Dimethyl-9, 10-Dihydro-8H-benzo [a] xanthen-11 (12H)-one-(CPDDHBXH)–Comparative analysis of macro and nano crystals*. *Mater. Today: Proc.* (2020).
26. K. Senthilkannan et al., *Tribological, filter studies of 3-Bromo-2-Hydroxy benzoic acid (BHBA) macro and nano crystals*. *Mater. Today: Proc.* (2020).
27. K. Senthilkannan et al., *Fluorescence, filter, nano tribological studies of 12-(4-Chlorophenyl)-9, 9-Dimethyl-9, 10-Dihydro-8H-Benzo [A] Xanthen-11 (12H)-One-(CPDDHBXH) macro and nano crystals*. *Mater. Today: Proc.* (2020).
28. K. Senthilkannan et al., *Tribological, Filter, FTIR and fluorescence studies of L-Alaninium tartrate (LAT) Macro and nano crystals*. *Mater. Today: Proc.* (2020).
29. G. Wilcox, *Clin. Biochem. Rev.* **26**, 19 (2005)
30. C.Y. Yang, Y.Y. Yen, K.C. Hung et al., *Nutr. Diabetes* **9**, 1 (2019). <https://doi.org/10.1038/s41387-019-0092-y>
31. R. Tundis, M.R. Loizzo, F. Menichini, *Mini Rev. Med. Chem.* **10**, 315 (2010). <https://doi.org/10.2174/138955710791331007>
32. S.O. Oyedemi, B.O. Oyedemi, Ijeh II, et al. *Sci. World J.* **1** (2017). <https://doi.org/10.1155/2017/3592491>
33. K. Khadayat, B.P. Marasini, H. Gautam et al., *Clin. Phytosci.* **6**, 1 (2020)
34. K. Kumar, K. Senthilkannan, R. Hariharasuthan, M. Jothibas, M. Vimalan, P. Baskaran, M. Iyanar, M. Kolanjinathan, *J. Mater. Sci. Mater. Electron.* **31**(23), 1 (2020). <https://doi.org/10.1007/s10854-020-04594-y>
35. L.J. Farrugia, *J. Appl. Cryst.* **45**, 849 (2012)

36. M. Kolanjinathan, K. Senthilkannan, S. Paramasivam, P. Baskaran, M. Iyanar, *Mater. Today: Proc.* **33**, 2750 (2020). <https://doi.org/10.1016/j.matpr.2020.01.575>
37. P. Periyathambi et al., Fluorescence and filter characterizations of NaBr-added L-alanine (LANB)—A comparative analysis in macro and nano scaled crystals. *Mater. Today: Proc.* (2020).
38. L. Selvaraj et al., Anti-diabetic (AD) studies of Bis Glycine Hydro Bromide—BGHB macro crystals milled to nano scale of 219 nm as the preliminary fine particles. *Mater. Today: Proc.* (2020).
39. G. Flora et al., Anti-diabetic (AD) and crystal stiffness characterizations of NaBr-added L-alanine (LANB)—A comparative analysis in macro and nano scale crystals. *Mater. Today: Proc.* (2020).
40. G. Flora et al., Anti-inflammatory (AI) and crystalline hardness characterisations of 4-(4-chlorophenyl)-7,7-dimethyl-7,8-dihydro-4h-1-benzopyran-2,5(3h,6h)-dione-CPDMDHHPHHD—Comparative analysis of macro and nano scales crystals. *Mater. Today: Proc.* (2020).
41. K. Senthilkannan et al., Anti diabetic (AD) studies of bis-glycine hydro bromide (45 nm) nano crystals. *Mater. Today: Proc.* (2020).
42. P. Saravanan et al., Biofriendly and competent domestic microwave assisted method for the synthesis of ZnO nanoparticles from the extract of *Azadirachta indica* leaves, *Mater. Today: Proc.* (2020).
43. K. SenthilKannan et al., Anti-diabetic (AD) activities of ZnO doped with Ce (7 at%) nano particles (NP). *Mater. Today: Proc.* (2020).
44. K. Senthilkannan et al., Anti-diabetic activities of ZnO doped with Ce (5 at%) nano particles (NPs). *Mater. Today: Proc.* (2020).
45. P. Baskaran et al., Anti-diabetic studies of barium paranitro phenolate macro and nano crystals. *Mater. Today: Proc.* (2020).
46. P. Baskaran et al., Anti-diabetic activities of ZnO doped with Ce (3 at%) nano particles. *Mater. Today: Proc.* (2020).
47. K. SenthilKannan et al., Anti diabetic (AD) studies of picolinium maleate nano crystals. *Mater. Today: Proc.* (2020).
48. K. SenthilKannan et al., Effect of anti microbial and fluorescence on L-Alaninium maleate (LAM) macro and nano crystals. *Mater. Today: Proc.* (2020).
49. K. SenthilKannan et al., Anti microbial and fluorescence activities of L-valinium picrate (LVP) macro and nano crystals. *Mater. Today: Proc.* (2020).
50. K. SenthilKannan et al., Photo catalytic, anti bacterial activities of Ce doped zinc oxide nano particles. *Mater. Today: Proc.* (2020).
51. V. Kalaipoonguzhali, Comparison of adsorption energy, ionization potential and electron affinity of CuS-ACT and CuS-Nit nanostructures monowire for nano device fabrication by computational approach. *Mater. Today: Proc.* (2020).
52. M. Kolanjinathan, Anti-diabetic studies of 4-(4-chlorophenyl)-7,7-dimethyl-7,8-dihydro-4H-1-benzopyran-2,5(3H,6H)-dione-(CPDMDHHPHHD) nanocrystals. *Mater. Today: Proc.* (2020).
53. K. SenthilKannan, Electronic transport, HOMO–LUMO and computational studies of CuS monowire for nano device fabrication by DFT approach. *Mater. Today: Proc.* (2020).
54. K. SenthilKannan, Anti diabetic (AD) activities of L-valinium picrate (LVP) macro and nano crystals. *Mater. Today: Proc.* (2020).
55. G. Flora, K. Senthilkannan, R. Rengarajan, P. Saravanan, *Mater. Today: Proc.* **33**, 4233 (2020). <https://doi.org/10.1016/j.matpr.2020.07.347>
56. M.S. Krishnamurthy, N. Shahina Begum, *Acta Crystallogr. E* **70**, 760 (2014).
57. R.P. Patel, K. SenthilKannan, R. Hariharasuthan, *Braz. J. Phys.* **51**, 339 (2021) <https://doi.org/10.1007/s13538-021-00883-x>
58. J.-Y. Zhang, X.-Y. Wang, M. Xiao, *Appl. Phys. Lett.* **81**, 2076 (2002). <https://doi.org/10.1063/1.1507613>
59. S.K. Kurtz, T.T. Perry, *J. Appl. Phys.* **39**, 3798 (1968). <https://doi.org/10.1063/1.1656857>
60. A. Von Hippel, E.P. Gross, J.G. Jelatis, M. Geller, *Phys. Rev.* **91**, 568 (1953). <https://doi.org/10.1103/PhysRev.91.568>
61. C. Hrizi, N. Chaari, Y. Abid, N. Chniba-Boudjada, S. Chaabouni, *Polyhedron* **46**, 41 (2012). <https://doi.org/10.1016/j.poly.2012.07.062>
62. A.C. Dhieb, A. Valkonen, M. Rzaigui, W. Smirani, *J. Mol. Struct.* **1102**, 50 (2015). <https://doi.org/10.1016/j.molstruc.2015.08.044>
63. R. Tundis, M.R. Loizzo, F. Menichini, *Mini. Rev. Med. Chem.* **10**, 315 (2010). <https://doi.org/10.2174/138955710791331007>
64. S.O. Oyedemi, B.O. Oyedemi, I.I. Ijeh, *Sci. World J.* **2017**, 1 (2017). <https://doi.org/10.1155/2017/3592491>
65. K. Khadayat, B.P. Marasini, H. Gautam, *Clin. Phytosci.* **6**, 1 (2020). <https://doi.org/10.1186/s40816-020-00179-8>
66. P. Baskaran, *Mater. Today: Proc.* **33**, 3051 (2020). <https://doi.org/10.1016/j.matpr.2020.03.268>
67. L.K. Williams, X. Zhang, S. Caner, *Nat. Chem. Biol.* **11**, 691 (2019)
68. S.K. Burley, H.M. Berman, C. Bhikadiya, *Nucleic Acids Res.* **47**, 464 (2019). <https://doi.org/10.1093/nar/gky1004>

69. W.L. DeLano, The PyMOL Molecular Graphics System (2020). <http://www.pymol.org>
70. S. Dallakyan, A.J. Olson, *Mol. Biol.* **1263**, 243 (2014). [https://doi.org/10.1007/978-1-4939-2269-7\\_19](https://doi.org/10.1007/978-1-4939-2269-7_19)
71. T.A. Halgren, *J. Comp. Chem.* **17**, 490 (1996)
72. BIOVIA, Dassault systemes, [Biovia Discovery studio Visualizer]. San Diego: Dassault systemes (2020)
73. A. Daina, O. Michielin, V. Zoete, *Sci. Rep.* **7**, 1 (2016). <https://doi.org/10.1038/srep42717>
74. M. Meena, C.K. Mahadevan, *Cryst. Res. Technol.* **43**(2), 166 (2007).
75. M. Meena, C.K. Mahadevan, *Arch. Appl. Sci. Res.* **2**, 185 (2010)
76. M. George, S.S. Nair, K.A. Malini, P.A. Joy, M.R. Anantharaman, *J. Phys. D Appl. Phys.* **40**, 1593 (2007)
77. A.A. Menazea, One-Pot Pulsed Laser Ablation route assisted copper oxide nanoparticles doped in PEO/PVP blend for the electrical conductivity enhancement (2020)
78. N. Sing, A. Agarwal, S. Sanghi, *Curr. Appl. Phys.* **11**, 783 (2011)
79. G. Catalan, D. O'Neill, R. M Bowman, and J.M. Gregg, *Appl. Phys. Lett.* **77**, 3078 (2000).
80. G. Catalan, *Appl. Phys. Lett.* **88**, 102902 (2006)
81. D. O'Neill, R.M. Bowman, J.M. Gregg, *Appl. Phys. Lett.* **77**, 1520 (2000).
82. S.A. Acharya, K. Singh, *Adv. Mat. Lett.* **5**, 61 (2014)
83. M. Jada Shanker, D. Buchi Suresh, Suresh Babu, *Mater. Today: Proc.* **3**, 2091(2016).
84. R. Divya, M. Meena, C.K. Mahadevan, C.M. Padma, *Int. J. Eng. Res. Appl.* **4**, 1 (2014)
85. Y.Y. Ma, F. Xiao, S. Ye, Q.Y. Zhang, Z. H. Jiang, *J. Am. Ceram. Soc.*, **96**(7), 2238 (2013). <https://doi.org/10.1111/jace.12314>
86. S. Hossain, *Electromagn. Biol Med.* **40**, 65 (2021). <https://doi.org/10.1080/15368378.2020.1850471>
87. D. Shyamala, R. Rathikha, K. Gomathi, *Int. J. Appl. Phys.* **12**, 35 (2016)
88. Suresh Sagadevan, et al. *Int. J. Chem. Tech. Res.* **6**, 2645 (2014).
89. P. Aji Udhaya, M. Meena. *Mater. Today: Proc.* **9**, 528 (2019).
90. S. Tamilselvan et al. *Spectrochim. Acta A Mol. Biomol.*, **114**, 19 (2013).
91. M. Meena, C.K. Mahadevan, *Mater. Lett.* **62**, 3742 (2008)
92. O. Mtioui, H. Litaïem, S. Garcia-Granda, L. Ktari, M. Dammak, *Ionics* **21**, 411 (2015)
93. Saïda Fatma Che´rif, Amira Che´rif, Wassim Dridi, Mohamed FaouziZid **13**, 5627 (2020)
94. B.G. Soares, M.E. Leyva, Barra, G.M.O., Khastgir, D, *Eur. Polym. J.* **42**, 676 (2006).
95. A. Langar, N. Sdiri, H. Elhouichet, M. Ferid, *Res. Phys.* **7**, 1022 (2017)
96. A. Oueslati, F. Hlel, K. Guidara, M. Gargouri, *J. Alloys Compd.* **492**, 508 (2010)
97. S.K. Tripathi, A. Gupta, M. Kumari, *Bull. Mater. Sci.* **35**, 969 (2012)
98. A. Dutta, T.P. Sinha, P. Jena, S. Adak, *J. Non-Cryst. Solids* **354**, 3952 (2008)
99. H. Bouaamlat, N. Hadi, N. Belghiti, H. Sadki, M.N. Ben-nani, F. Abdi, T. Lamcharfi, M. Bouachrine, and M. Abarkan, *Adv. Mater. Sci.* (2020).
100. B. Chatterjee, P.N. Gupta, *Non-Cryst. Solids.* **358**, 3355 (2012)
101. A.R. James, S. Priya, K. Uchino, K.J. Srinivas, *Appl. Phys.* **90**, 3504 (2001)
102. K. Momma, F. Izumi, *J. Appl. Crystallogr.* **44**, 1272 (2011)
103. P.R. Spackman, M.J. Turner, J.J. McKinnon, S.K. Wolff, D.J. Grimwood, D. Jayatilaka, M.A.J. Spackman, *Appl. Cryst.* **54**(3), 1006 (2021)

**Publisher's Note** Springer Nature remains neutral with regard to jurisdictional claims in published maps and institutional affiliations.

Springer Nature or its licensor holds exclusive rights to this article under a publishing agreement with the author(s) or other rightsholder(s); author self-archiving of the accepted manuscript version of this article is solely governed by the terms of such publishing agreement and applicable law.